Journal of Molecular Graphics and Modelling 45 (2013) 13–25

Contents lists available at ScienceDirect

Journal of Molecular Graphics and Modelling

journal homepage: www.elsevier.com/locate/JMGM

Theoretical studies on the binding of rhenium(I) complexes to inducible nitric oxide synthase

Bruno L. Oliveira[a,**], Irina S. Moreira[b], Pedro A. Fernandes[b], Maria J. Ramos[b], Isabel Santos[a], João D.G. Correia[a,*]

[a] Unidade de Ciências Químicas e Radiofarmacêuticas, IST/ITN, Instituto Superior Técnico, Universidade Técnica de Lisboa, Estrada Nacional 10, 2686-953 Sacavém, Portugal

[b] REQUIMTE, Departamento de Química e Bioquímica, Faculdade de Ciências da Universidade do Porto, Rua do Campo Alegre s/n, 4169-007 Porto, Portugal

ARTICLE INFO

Article history:
Accepted 30 July 2013
Available online 11 August 2013

Keywords:
Nitric oxide synthase
Technetium
Rhenium
Docking
Molecular dynamics
Free energy perturbation calculations

ABSTRACT

Considering our interest in the design of innovative radiometal-based complexes for *in vivo* imaging of nitric oxide synthase (NOS), we have recently introduced a set of $M(CO)_3$-complexes (M = ^{99m}Tc, Re) containing a pendant N^{ω}-NO_2-L-arginine moiety, a known inhibitor of the enzyme. Enzymatic assays with purified inducible NOS have shown that the non-radioactive surrogates with 3-(**Re1**; K_i = 84 μM) or 6-carbon linkers (**Re2**; K_i = 6 μM) are stronger inhibitors than the respective metal-free conjugates **L1** (K_i = 178 μM) and **L2** (K_i = 36 μM), with **Re2** displaying the highest inhibitory potency. Aiming to rationalize the experimental results we have performed a molecular docking study combined with molecular dynamics (MD) simulations and free energy perturbation (FEP) calculations. The higher inhibitory potency of **Re2** arises from the stronger electrostatic interactions observed between the "$Re(CO)_3$" core and the residues Arg260 and Arg382. This interaction is only possible due to the higher flexibility of its C6-carbon spacer, which links the N^{ω}-NO_2-L-arginine moiety and the "$Re(CO)_3$" organometallic core. Furthermore, FEP calculations were carried out and the resultant relative binding energies ($\Delta\Delta G^{calc}_{bind}$ = 0.690 ± 0.028 kcal/mol, **Re1**/**L1** and 1.825 ± 0.318 kcal/mol, **Re2**/**L2**) are in accordance with the experimental results ($\Delta\Delta G^{exp}_{bind}$ = 0.461 ± 0.009 kcal/mol, **Re1**/**L1** and 1.129 ± 0.210 kcal/mol, **Re2**/**L2**); there is an energetic penalty for the transformation of the Re complexes into the ligands and this penalization is higher for the pair **Re2**/**L2**.

1. Introduction

Nitric oxide (NO) is an endogenous free radical that results from the catalytic oxidation of L-arginine (L-Arg) to L-citrulline (L-Cit) by the heme-containing enzyme nitric oxide synthase (NOS), which has three distinct isoforms: endothelial (eNOS), neuronal (nNOS) and inducible (iNOS). They differ in tissue distribution and biological role. The eNOS and nNOS are constitutively expressed and are calcium/calmodulin dependent. Under normal physiological conditions, these isoforms generate low transient levels of NO (100–500 nmol/mg of NOS min) in response to the increase in intracellular Ca^{2+} concentrations. These low levels of NO regulate blood pressure, platelet aggregation and neurotransmission [1,2]. The iNOS is expressed and induced at a transcriptional level by inflammatory stimuli (*e.g.* interferon, IFN-γ and bacterial lipopolysaccharide, LPS) and is calcium independent. This isoform can generate high amounts of NO (up to 1.5 μmol/mg of NOS min), which can cause cellular cytotoxicity and tissue damage. The overexpression of iNOS is thought to contribute to the pathophysiology of several diseases, such as stroke, hypertension, cancer, ischemia, inflammation, colitis, and rheumatoid arthritis [1–3]. Imaging of NO/NOS expression would allow earlier diagnosis, earlier treatment and individualized patient management in the clinical set. Considering our interest in the design of innovative radioactive probes for *in vivo* targeting of NOS by the nuclear imaging technique Single Photon Emission Computed Tomography (SPECT), we have recently introduced a set of $^{99m}Tc(CO)_3$-complexes containing NOS-recognizing units (*e.g.* L-Arg derivatives, guanidino or S-methylisothiourea moieties) [4–6]. Enzymatic activity of iNOS in the presence of the $Re(CO)_3$-complex analogs, prepared as "non radioactive" surrogates, have shown that **Re1** (K_i = 84 μM) and **Re2** (K_i = 6 μM), which contain the N^{ω}-NO_2-L-Arg inhibitor, still presented inhibitory action (Fig. 1).

* Corresponding author. Tel.: +351 219946233.
** Corresponding author. Current address: A. A. Martinos Center for Biomedical Imaging, Massachusetts General Hospital and Harvard Medical School, 149 13th Street, Suite 2301, Charlestown, MA 02129, USA.
E-mail addresses: oliveira@nmr.mgh.harvard.edu (B.L. Oliveira), jgalamba@itn.pt (J.D.G. Correia).

1093-3263/$ – see front matter © 2013 Elsevier Inc. All rights reserved.
http://dx.doi.org/10.1016/j.jmgm.2013.07.007

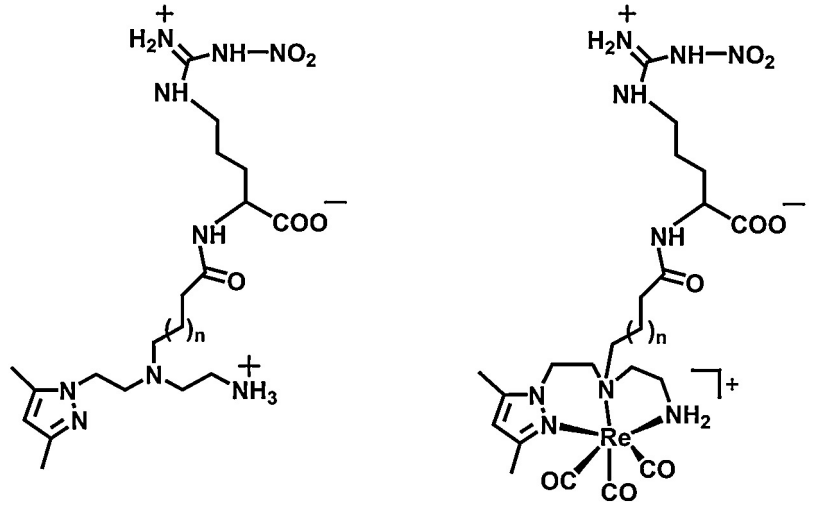

Fig. 1. Organometallic complexes of the type *fac*-[Re(CO)$_3$(k^3-L)] (L = **L1** and **L2**) containing a pendant N$^\omega$-NO$_2$-L-arginine moiety.

Indeed, **Re1** and **Re2** are the first examples of organometallic complexes able to inhibit the iNOS. Interestingly, the rhenium complexes presented higher inhibitory potency than the respective metal-free conjugates **L1** (K_i = 36 μM) and **L2** (K_i = 178 μM) (Fig. 1). Moreover, **Re2** displayed the highest inhibitory potency, which is comparable to that of free non-conjugated N$^\omega$-NO$_2$-L-Arg (K_i = 3–8 μM) [5].

Both Re(I) complexes permeate through macrophage cell membranes and interact with the cytosolic target enzyme, as confirmed by the inhibition of NO biosynthesis in LPS-induced macrophages. Improvement of the inhibitory effect after metal coordination was also observed in this cell model [5]. Aiming to shed light on the specific protein (iNOS)/ligand (rhenium complexes) interactions and to establish a preliminary structure-activity relationship, we have performed a molecular docking study to evaluate the binding modes of the N$^\omega$-NO$_2$-L-Arg-containing ligands (**L1** and **L2**) and the corresponding rhenium complexes (**Re1** and **Re2**). Molecular dynamics simulations were used to refine the conformations obtained by docking and to identify the most prevalent interactions between the Re complexes and the iNOS isoform. The relative binding energy between the pairs **Re1**/**L1** and **Re2**/**L2** bound to iNOS were also evaluated by free energy perturbation calculations.

2. Results and discussion

2.1. Docking calculations

We have used the AutoDock software to dock the inhibitors **L1**, **L2**, **Re1** and **Re2** into the iNOS isoform. In order to identify important residues for iNOS ligand binding we used the LIGPLOT [7] program to generate schematic diagrams of the protein-ligand interactions observed in some X-ray structures published in the Brookhaven Protein Databank. Crystal structures of the heme oxygenase domain of iNOS complexed with the substrate L-Arg (**1**, pdb id 1NOD) [8], with a variety of L-Arg derivatives like N$^\omega$-OH-L-Arg (**2**, pdb id 1DWV) [9], N$^\omega$-propyl-L-Arg (**3**, pdb id 1QW4) [10], L-thiocitrulline (**4**, pdb id 3NOD) [9] and 4-fluoro-iminoethyl-L-lysine (**5**, pdb id 1R35) [11], as well as with non L-Arg derivatives (*e.g.* **11**, pdb id 3EAI) [12] have been used in this study (Figs. S1–S3, figures labeled "S" are in Supporting Information). For the sake of example, Fig. 2A displays a LIGPLOT diagram showing the interactions observed between N$^\omega$-propyl-L-Arg and the binding site residues of iNOS. A thorough analysis of the various LIGPLOT diagrams, has shown that in most cases the nitrogen atoms of the guanidine/amidine moieties are bound by two H-bonds to Glu371 and one H-bond to Trp366 (Fig. 2B).

Additionally, the α-amine group also forms an H-bond with one of the Glu371 carboxylate O atoms, whereas the carboxylate group of the amino acid function interacts by means of H-bonds with Tyr341 and Tyr367. These residues seem to give an important contribution for stabilizing the L-Arg derivatives and were considered fully flexible during the docking process of **L1**, **L2**, **Re1** and **Re2**. Although Gln257 does not always interact with the various inhibitors, this residue has been shown to have different conformations in several crystal structures, which have also been carefully explored through flexible protein-ligand docking [12,13]. The binding site residues of iNOS considered flexible during the docking process are shown in Fig. 2C.

Several studies demonstrated that, although the dimer is biologically meaningful for the correct function of the enzyme, it is still possible to affect the iNOS specificity by modifying the microenvironment of the active center of the monomer: (i) Xue et al. have used docking studies at the monomer to drive the experimental design of new inhibitors to nNOS [14]; (ii) Maccallini et al. have also performed molecular docking on the monomer to obtain selective inhibitors of iNOS [15]; (iii) Francis et al. have used the monomer to design and dock new scaffolds with higher selectivity for iNOS isoform [16]; (iv) Aparna et al. have also used MD simulation of the monomer to study the specificity of various inhibitors of the iNOS enzyme [17] Recently, we have also clearly shown that the iNOS monomeric form fulfills the requirements needed for studying the structural factors of the active site that account for the different behavior of closely related compounds, which is the main goal of this work [13]. Docking studies were performed using the 3D-structure information of the heme oxygenase domain of iNOS obtained from the 1QW4 crystal structure (monomer A). The most straightforward way to validate the accuracy of a docking procedure is to determine if it is able to correctly reproduce the experimental binding pose. For validation of our docking conditions, besides the L-Arg derivatives **1**–**5**, we have also selected non-amino acid compounds from different families of NOS inhibitors like isothiourea- (**6**, pdb id 1DF1) [18], acetamidine- (**7**,

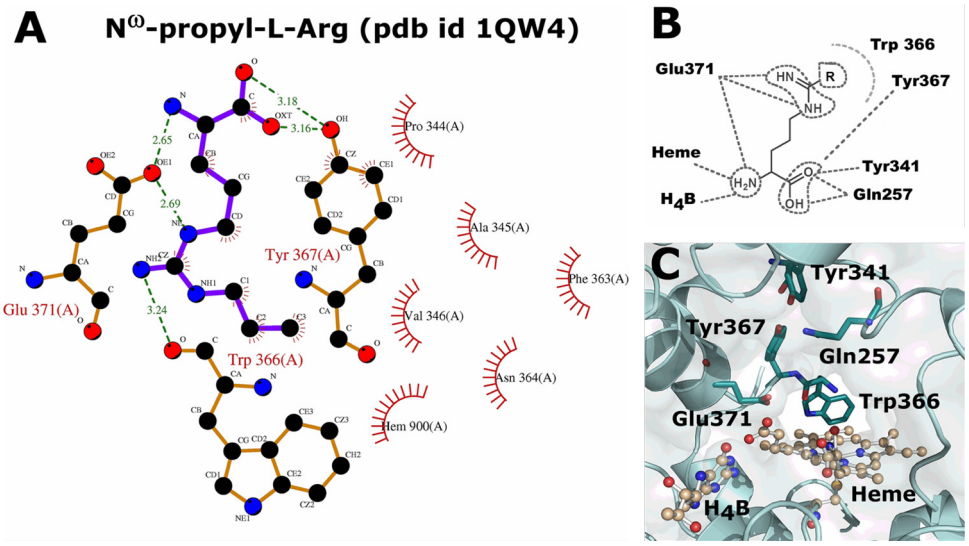

Fig. 2. (A) LIGPLOT diagram depicting interactions between the inhibitor Nω-propyl-L-Arg and the binding site residues of iNOS. The inhibitor is shown in blue and the protein micro-environment is shown in orange. The atoms are color coded (carbon, black; oxygen, red; nitrogen, blue). Hydrogen bonds are presented as green dashed lines with distances in Å. Residues in hydrophobic contact with the inhibitor are represented by red semicircles. (B) Interactions considered important for stabilization of compounds analogs of L-arginine. (C) Binding site residues of iNOS considered flexible during the docking process. (For interpretation of the references to color in this figure legend, the reader is referred to the web version of the article.)

pdb id 1QW5) [10], coumarin- (**8**, pdb id 2BHJ) [19], nitroindazole- (**9**, pdb id 1M8E) [20], quinazoline- (**10**, pdb id 3E7T) [12] and aminopyridine-based inhibitors (**11**, pdb id 3EAI) [12] (Fig. S1). Compounds **10** and **11** are potent and highly selective inhibitors of iNOS, being included in the class of compounds that extend out of the enzyme binding site where large structural differences among the NOS isoforms are found [12]. All small molecules were extracted in the conformation found in the crystal structures and re-docked into the corresponding binding pocket with the aim of determining the ability of AutoDock to reproduce the orientation and position of the inhibitors observed in the crystal structures.

The root-mean-square-deviation (RMSD) between the X-ray and the docked structures for the eleven compounds ranged between 1.03 and 2.90 Å (Table S1). As an illustrative example, Fig. 3 displays the docked conformations obtained for inhibitors **3**, **7** and **10**, which were compared with the corresponding X-ray conformations. Docking results for the remaining molecules are presented in Fig. S4. Brought together, analysis of the results confirm that the docking conditions reproduce the experimental binding modes of the selected small molecules.

After validation of the docking model we have docked **L1**, **L2**, **Re1** and **Re2** inside the active pocket of iNOS. Firstly, the docking results were evaluated using as criteria the ability of AutoDock to place the common pendant Nω-NO_2-L-Arg moiety over the heme unit and, secondly, to reproduce the conformation of Nω-NO_2-L-Arg in the crystal structure of Nω-NO_2-L-Arg complexed with nNOS (pdb id 1K2R). In the first set of conditions the compounds were considered fully flexible, and the results obtained were unsatisfactory, most likely due to the large size and high flexibility of the molecules. A second set of docking simulations was conducted considering some rotatable bonds of **L1**, **L2**, **Re1** and **Re2** (Fig. S5) rigid. More precisely, the pendant Nω-NO_2-L-Arg moiety was locked in the same conformation found in the X-ray (pdb id 1K2R). Fig. 4 shows the four lowest-energy conformations obtained for **L1**, **L2**, **Re1** and **Re2** inside the iNOS isoform. Figs. S6 and S7 present the top 10 lowest-energy conformations obtained for the docking of **L1** and **Re1**.

In general, the binding modes obtained by docking the Nω-NO_2-L-Arg-containing compounds resemble the binding mode of free Nω-NO_2-L-Arg found in the crystal structure of Nω-NO_2-L-Arg:nNOS (pdb id 1K2R). The Nω-NO_2-L-Arg moiety of **L1**, **L2**, **Re1** and **Re2** is situated near the Fe atom and almost parallel to the heme group. However, some peculiarities were found: docking results for **L1** and **L2** revealed that, in the lowest energy cluster, two different binding modes are preferred. In one of them, the ligands are placed above the heme group with the Nω-NO_2-L-Arg moiety anchored by the Glu371 of the active site (Fig. 4A and B). In the second binding mode the ligand is "flipped" and, instead of the Nω-NO_2-L-Arg moiety, the pyrazole ring is placed over the heme group (Fig. S6).

For **Re1** and **Re2**, the best-docked conformations share a similar binding mode, with the complexes being anchored in the active site through a bidentate interaction between the NO_2-guanidine moiety and Glu371 of the enzyme (Fig. 4A′ and B′). The flexible tail of the complexes is extended above the heme propionate arms, with the "$ReCO_3$" core interacting with Arg260 and Arg382. The amine of the chelator interacts with the CO group of the H_4B cofactor. Interestingly, comparison of the data obtained for **L1**/**L2** and **Re1**/**Re2** has shown that in the case of the rhenium complexes there is a higher number of docked conformations where the NO_2-guanidine moiety is placed over the heme group (Figs. S6 and S7). These results suggest that the metal center plays a key role in the organization and orientation of the organic ligands inside the active pocket of iNOS.

2.2. Molecular dynamics simulations

Docking results are often affected by slight conformational changes of the protein residues. Therefore, aiming to overcome the shortcomings generally associated to docking studies, we have re-evaluated the interactions of **L1**, **L2**, **Re1** and **Re2** with iNOS using further MD simulations. The MD simulations allow to relax the docked complexes and therefore to examine structural changes expected to occur in the iNOS binding pocket due to the binding of the sterically bulky rhenium complexes. Furthermore, these MD simulations results can be used as predictive tools to identify structural modifications that might improve the binding properties of rhenium complexes bearing pendant Nω-NO_2-L-Arg derivatives.

MD simulations were performed to refine and optimize the conformations of **L1**, **L2**, **Re1** and **Re2** chosen from the docking studies.

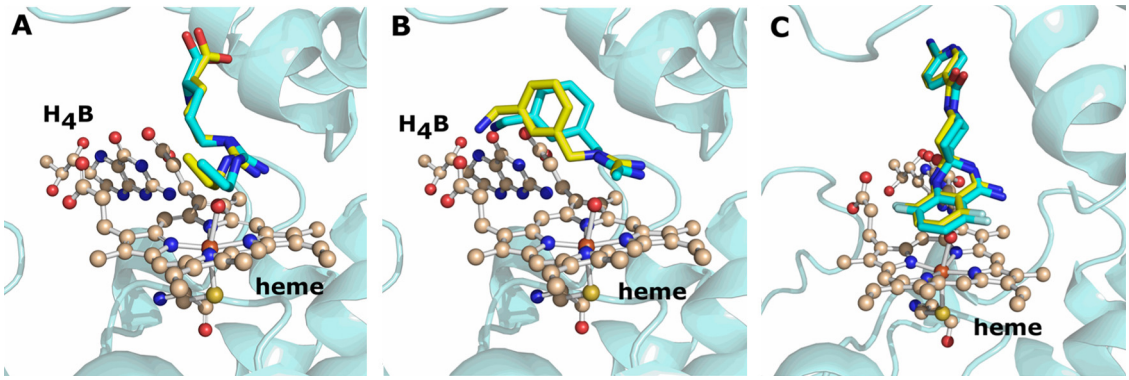

Fig. 3. Binding modes obtained by docking inhibitors **3**, **7** and **10** inside iNOS. Inhibitors are shown in cyan sticks (predicted binding conformation) or in yellow sticks (X-ray binding conformation). The heme group and the H_4B cofactor are shown in ball and stick representation. Nitrogen, oxygen, sulfur, fluor and iron atoms are depicted in blue, red, yellow, light blue and orange, respectively. H-atoms are omitted for clarity. The same representation will be used in the following figures. (For interpretation of the references to color in this figure legend, the reader is referred to the web version of the article.)

The 3D-structure of iNOS used in the simulations was taken from pdb 1QW4 [10] because of its reasonable resolution (2.4 Å) and intact X-ray structure. The MD simulations were set up as described in the Methods section and in reference [13].

2.3. Structural stability during MD simulations

The RMSD of the backbone with respect to the initial structures were calculated along the MD trajectories to assess the stability of the systems. RMSDs were computed for **L1**, **L2**, **Re1** and **Re2**, and for the respective iNOS complexes. As an example, the RMSD values for **Re1**, **Re2**, **Re1**:iNOS are **Re2**:iNOS are presented in Fig. 5A and B.

The **Re1**:iNOS and **Re2**:iNOS systems (Fig. 5A and B) appear to have reached a plateau after 1.5–2 ns of equilibration, where the RMSD converged to a value around ~2.0–2.5 Å, indicating that 8 ns simulation is probably enough for stabilization. To investigate the dynamic features in the binding of the compounds, RMSD was also monitored along the MD trajectories for the **Re1** and **Re2** complexes (Fig. 5A and B). The RMSD plots show that **Re1** and **Re2** underwent conformational changes at the active site of iNOS relative to the initial position obtained from the dockings (Fig. 5A and B). Such behavior can be explained based on the flexibility associated to the 3- or 6-carbon alkyl spacers as can be concluded by the analysis of the RMSD of the C3- and C6-organometallic moieties displayed in Fig. 5A′ and B′.

To check for conformational changes in the binding mode of **Re1** and **Re2** inside the active pocket of iNOS MD snapshots of the **Re1**:iNOS and **Re2**:iNOS complexes were selected every 0.2 ns and superimposed on the initial structure. As shown in Fig. 6A, the

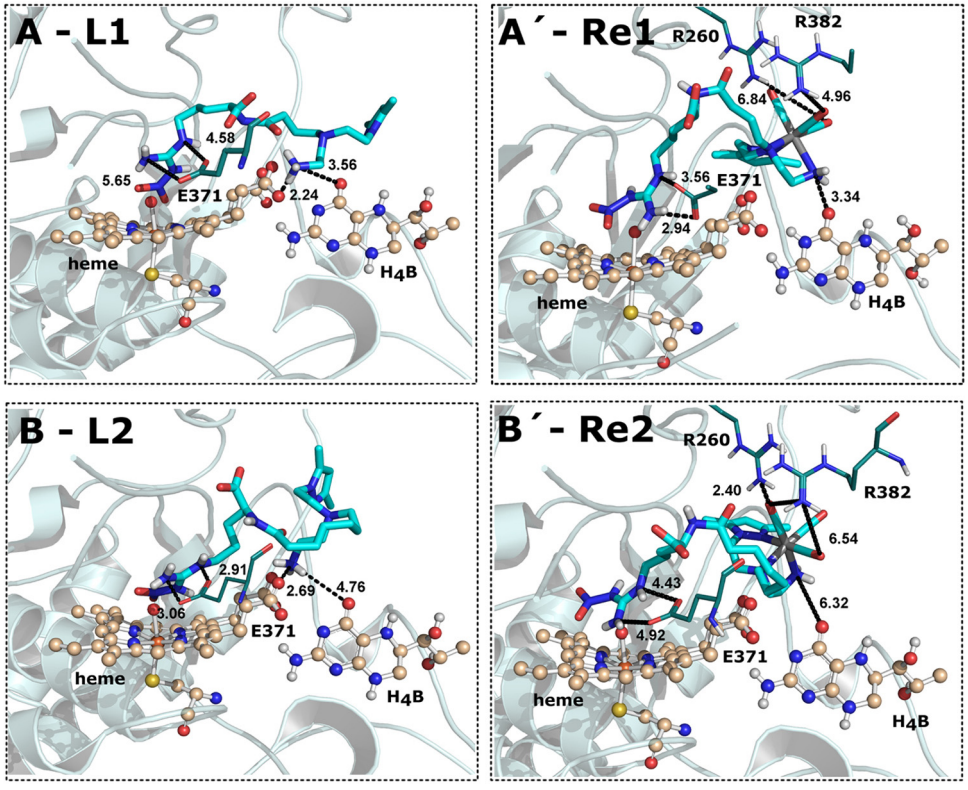

Fig. 4. Lowest-energy conformations of the docked inhibitors **L1** (A), **Re1** (A′), **L2** (B) and **Re2** (B′). All distances shown in Å.

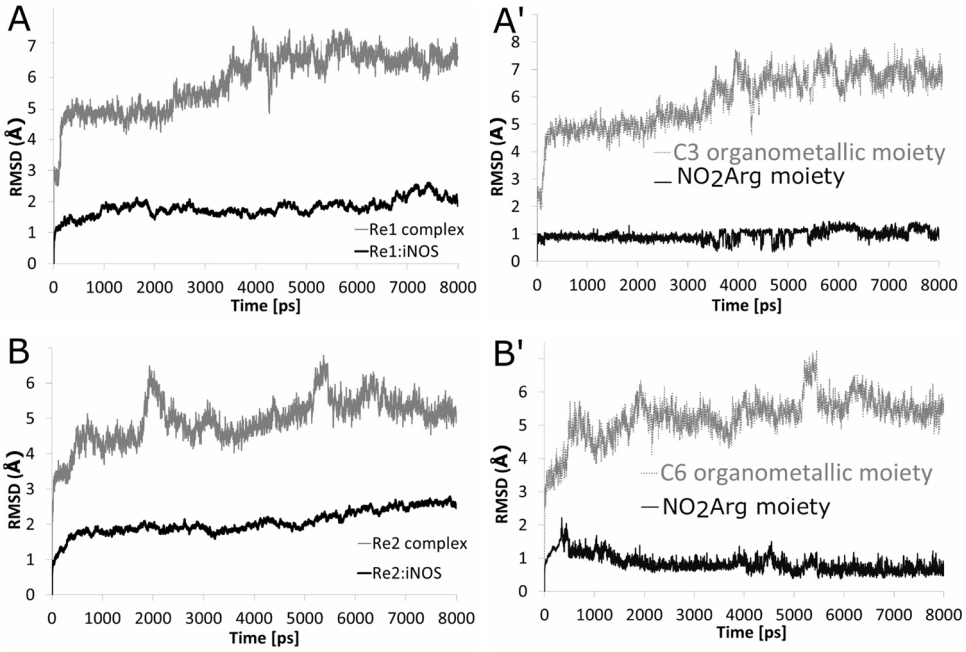

Fig. 5. RMSD of the systems **Re1** and **Re1**:iNOS (A); **Re2** and **Re2**:iNOS (B) during 8 ns simulation. Panels A′ and B′ depict the RMSD of the spacers (C3 or C6) and N^{ω}-NO_2-L-Arg moiety for **Re1** and **Re2**.

location of the organometallic core of **Re1** changes significantly after MD refinement, which is in accordance with the previous calculated RMSD values (Fig. 5A′).

In the case of **Re2** the simulation has shown a smaller shift in the location of the "$Re(CO)_3$" core (Figs. 5B′ and 6B). Additionally, the simulations also revealed that the N^{ω}-NO_2-L-Arg moiety occupies in all cases the expected binding site, being stable throughout the simulation (Figs. 5A′, B′ and 6).

2.4. Binding modes of *L1*, *L2*, *Re1* and *Re2* in iNOS isoform

Common features can be found in the binding modes of **L1**, **Re1** and **Re2** inside iNOS. The compounds are anchored in the active site through a bidentate interaction between the nitrogen atoms (Nε, Nη1) of the NO_2-guanidine moiety and the oxygen atoms of the CO_2^- of the Glu371 residue (Fig. 7). The H-bonds involved are relatively short [d(Nε···OE1) = 2.68 ± 0.09 Å and d(Nη1···OE2) = 2.72 ± 0.10 Å for **L1**:iNOS; d(Nε···OE1) = 2.82 ± 0.13 Å and d(Nη1···OE2) = 2.80 ± 0.12 Å for **Re1**:iNOS; d(Nε···OE1) = 3.03 ± 0.16 Å and d(Nη1···OE2) = 2.85 ± 0.14 Å for **Re2**:iNOS]. This critical H-bonding network plays a key role in keeping the inhibitors over the heme unit, probably stabilizing the inhibitors inside the active pocket of iNOS. This stable interaction is most likely responsible for the lower RMSD values found for the N^{ω}-NO_2-L-Arg moiety, as exemplified in Fig. 5 for **Re1** and **Re2**. The carbonyl group of the residue Trp366 interacts with the Nη1 atom of the NO_2-guanidine moiety, also assisting in the positioning of the inhibitors. In contrast, **L2** underwent a remarkable change during the MD simulation as shown in Fig. 7B. In fact, the inhibitor adopted a curled conformation in iNOS instead of the extended conformation found for **L1**, **Re1** and **Re2**. In the case of **L2**, the H-bond interactions between the NO_2-guanidine moiety and the CO_2^- of the Glu371 residue, are no longer present [d(Nε···OE1) = 8.71 ± 1.44 Å, d(Nη1···OE2) = 8.23 ± 1.69 Å for **L2**:iNOS] and the NO_2-guanidine moiety is closer to the heme propionates arms (Fig. 7B).

Our previous enzymatic studies have demonstrated that conjugation of N^{ω}-NO_2-L-Arg to the pyrazolyl-diamine chelating unit affected negatively their binding to the active site of iNOS. In fact, we have found K_i values significantly higher for **L1** (178 μM) and **L2** (36 μM) than for the corresponding free inhibitor (3 μM). More recently, MD simulations performed with iNOS complexed with N^{ω}-NO_2-L-Arg have shown that the affinity of this inhibitor for iNOS can be most likely attributed to strong H-bonds formed between the α-NH_3^+ of N^{ω}-NO_2-L-Arg and the CO_2^- group of the heme propionate A [13]. The conjugation of N^{ω}-NO_2-L-Arg, through the α-NH_3^+ group, to the pyrazolyl-diamine ligand prevents this interaction, leading to inhibitors with lower affinity for the enzyme.

Since water molecules can play an important role in ligand binding, water-mediated interactions between **L1**/**L2** and iNOS were checked aiming to rationalize the differences found in the binding affinities. The most conserved water molecules that persist during the last 3 ns of simulation of **L1**:iNOS (A) and **L2**:iNOS (B) are shown in Fig. 8.

Despite the presence of conserved water molecules in the binding pockets of both **L1**:iNOS and **L2**:iNOS complexes, the H-bond networks showed some differences. In **L2**:iNOS the water molecules at the binding site mediate H-bonds between each side-chain of the important polar residues Arg260, Asp274, and Arg382 and the primary amine of **L2**, contributing most probably, for its better affinity (**L1**, 178 μM and **L2**, 36 μM). Additionaly, various water molecules intensify the interaction between the NO_2-Arg moiety and the heme propionate arms, which are essential for stabilization of L-Arg, preventing in this way the binding of the substrate.

Metallation of **L1** and **L2** yielded complexes **Re1** (K_i = 84 μM) and **Re2** (K_i = 6 μM), respectively, which are stronger inhibitors than the corresponding free ligands. The improvement in the affinity is more evident when the spacer length between the NO_2-Arg moiety and the metal fragment increases (**Re1** *versus* **Re2**). The longer linker in the **Re2** seems to provide more flexibility to the molecule allowing the accommodation of the "$Re(CO)_3$" core near the Arg260 and Arg382 residues. For **Re1**, the bulky organometallic moiety is oriented toward the peripheral C1 pocket (Met114, Asn115, Pro116, Thr120 and Tyr485) at the edge of the active site, preventing the interactions found for **Re2** (Fig. S8). However, the hydrophobic contacts between Met114, Pro116, Thr120 and Tyr485 and the pyrazole

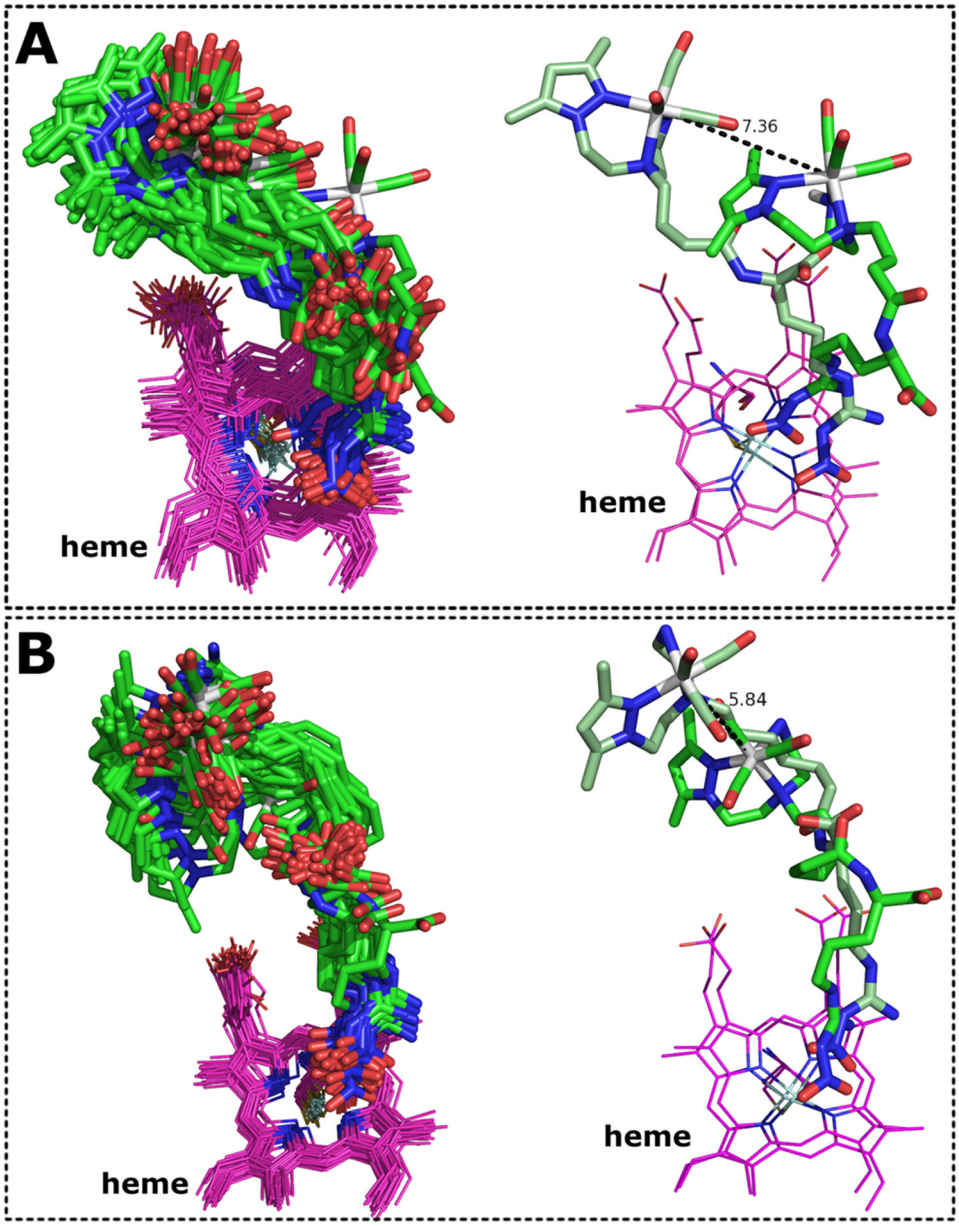

Fig. 6. Left panel: 3D structures of the **Re1**:iNOS (A) and **Re2**:iNOS (B) complexes observed along 8 ns of MD simulation. MD snapshots were selected every 0.2 ns and superimposed using heavy atoms. Right panel: superimposition of snapshots at 0 ns and 8 ns of simulation of the complexes **Re1**:iNOS (A) and **Re2**:iNOS (B). The starting structure is represented in green sticks and the last structure from the MD simulation is represented in pale green sticks. Protein and hydrogen atoms are omitted for clarity.

group of **Re1**, combined with the interactions between the protein and the N^{ω}-NO_2-L-Arg moiety, correlate well with the reasonable affinity found for this complex (K_i = 84 μM).

The volumes of the free inhibitors **L1**, **L2**, **Re1** and **Re2** as well as the volume of the active site cavities for **L1**:iNOS, **L2**:iNOS, **Re1**:iNOS and **Re2**:iNOS were calculated using the in-house VolArea software [21], and the following average results were obtained: **L1**, 352.42 ± 0.43 Å^3; **L2**, 396.11 ± 0.32 Å^3; **Re1**, 429.26 ± 0.57 Å^3; **Re2**, 437.09 ± 0.53 Å^3; **L1**:iNOS, 2444.09 ± 50.19 Å^3; **L2**:iNOS, 3321.37 ± 62.59 Å^3; **Re1**:iNOS, 2330.15 ± 30.04 Å^3; **Re2**:iNOS, 2253.49 ± 22.07 Å^3. The smaller volume of the active site of **Re2**:iNOS combined with the larger volume of **Re2** suggest an increased complementarity of shape and charge (Fig. 9).

Brought together, our results suggest that the metal center plays a key role in the organization and orientation of the organic ligands, and thus defining the overall shape of the inhibitors that fit better in the active pocket of iNOS. Such situation results in stronger van der Waals interactions between rhenium complexes and iNOS, which most probably accounts for their better affinity toward iNOS. Moreover, several recent studies suggest that conformational entropy might contribute significantly to binding affinity. Changes in the conformational entropy of the ligand, upon binding, have been investigated, underlining the advantage of designing conformationally restricted ligands [23–27]. The structurally restricted conformations of the rhenium complexes may also contribute for their higher affinity.

To get further insights into the binding affinity differences found for **Re1** and **Re2**, for each MD trajectory, we have calculated the electrostatic interaction energies between the "Re$(CO)_3$" core and Arg260 and Arg382, using the NAMD [28] energy plugin of VMD [29] (Fig. 10). We found more favorable electrostatic interactions for **Re2** than for **Re1**, which support the binding affinity experimental data (K_i of **Re2** > K_i of **Re1**) [5].

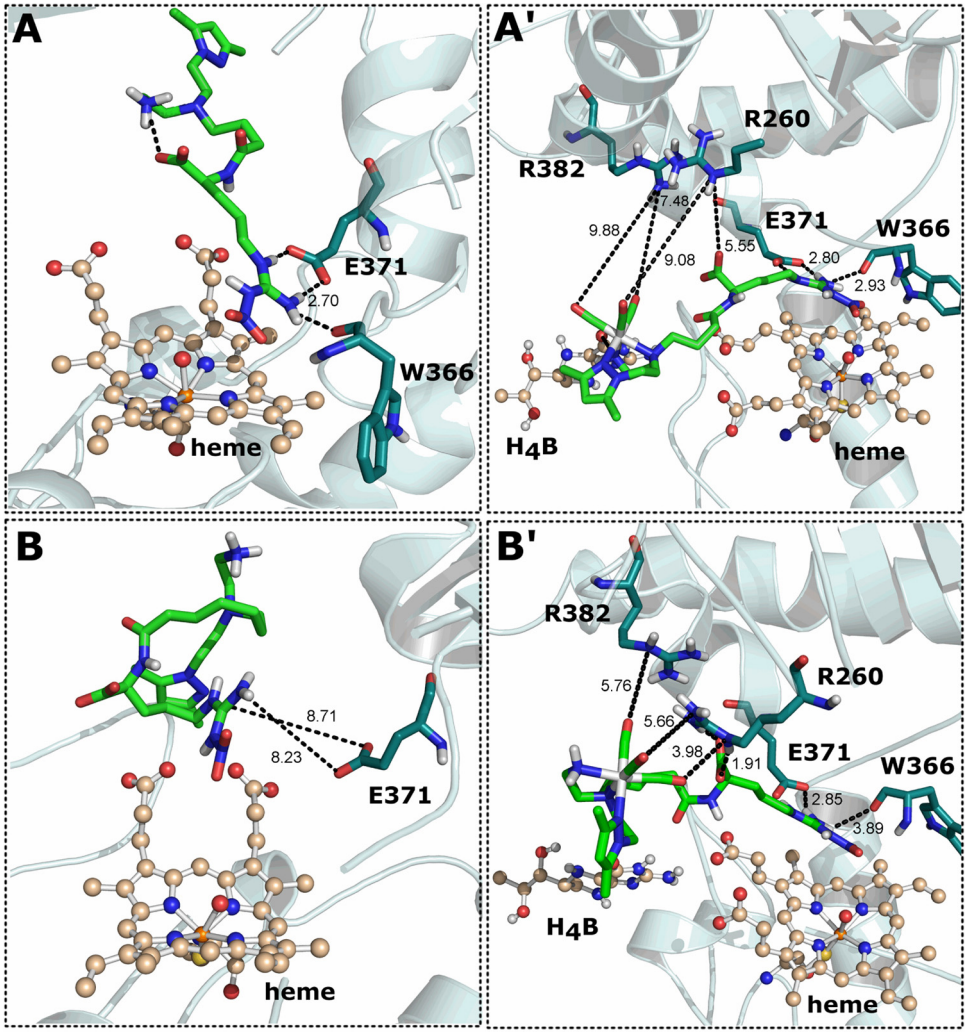

Fig. 7. Structural micro-environment around the active site of the average structures of the systems **L1**:iNOS (A), **Re1**:iNOS (A′), **L2**:iNOS (B) and **Re2**:iNOS (B′). All distances shown in Å.

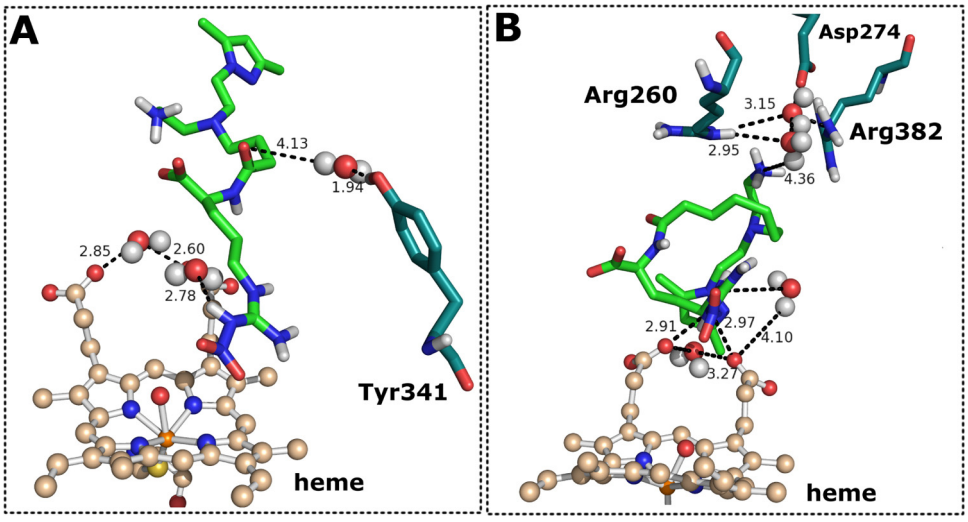

Fig. 8. Hydrogen bond networks stabilizing **L1** (A) and **L2** (B) within the iNOS binding pocket. The buried water molecules shown in red spheres do not exchange and persist throughout the last 2 ns of the simulation. All distances shown in Å. (For interpretation of the references to color in this figure legend, the reader is referred to the web version of the article.)

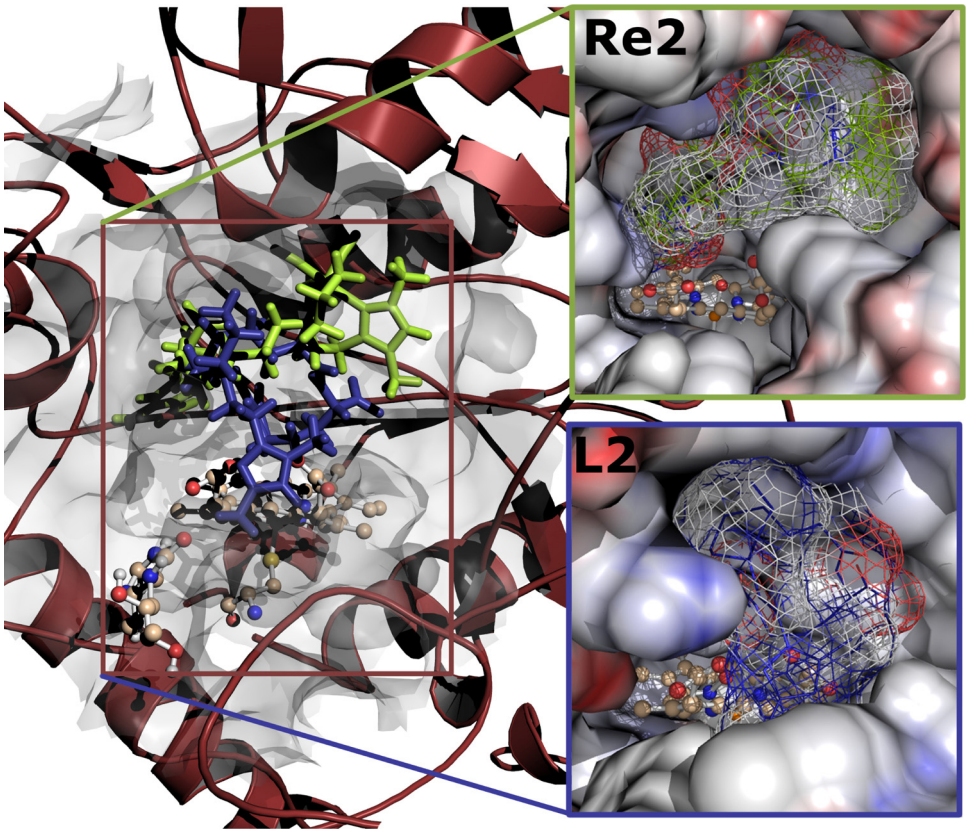

Fig. 9. Molecular surfaces of the active site of the complexes **L2**:iNOS and **Re2**:iNOS colored according to electrostatic potential. This figure was generated using the VASCo PyMOL plug-in [22].

2.5. Free energy calculations

To validate our simulations and gain a deeper insight into the influence of the "$Re(CO)_3$" core in the affinity of the complexes, we have used the Alchemical Free Energy Perturbation method (FEP) within the NAMD software to calculate the free energy difference for the pairs **Re1**/**L1** and **Re2**/**L2** bound to iNOS (Fig. 11) [30–32].

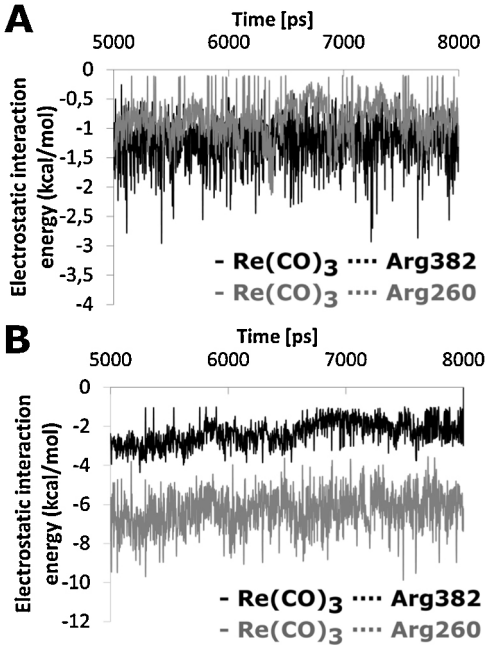

Fig. 10. Electrostatic interaction energy observed between the "$Re(CO)_3$" core and the iNOS residues Arg260 and Arg382, calculated for the last 3 ns of simulation: **Re1**:iNOS (A) and **Re2**:iNOS (B).

The average structures of the complexes **Re1**:iNOS and **Re2**:iNOS calculated for the last 3 ns of simulation were used as starting point for the alchemical transformations. Rather than using equally spaced windows, within the FEP calculations, more windows were constructed in the end regions of the simulations, to ensure adequate sampling (32 windows between $\lambda = 0$ and $\lambda = 1$, see the Methods section). At each window, the system was equilibrated for 24 ps, followed by 240 ps of accumulation (8.45 ns, optimized conditions). The transformations were carried out in solution, and within the protein environment. In each case, both the forward ($\lambda = 0 \rightarrow 1$) and the backward transformations ($\lambda = 1 \rightarrow 0$) were performed, with the final coordinates for the forward transformation used as the starting point of the backward simulation. Considering the simulations in both free and bound states, as well as in the forward and backward directions, the total time of simulation was ~33 ns.

Representative free energy differences obtained by FEP for the transformation of **Re1** into **L1** and **Re2** into **L2**, both in solution and bound to the protein, are depicted in Fig. 12.

To assess the accuracy of our calculations, the results were compared with the experimental binding data and the values found are shown in Table 1.

As an example, the free energy for the mutation of **Re2** into **L2** in solution (ΔG_{solv} Re → L) was −32.57 kcal/mol, while bound to the protein (ΔG_E Re → L) was -30.52 kcal/mol. These values have no meaning by themselves, but the difference between them (2.05 kcal/mol) is the difference in the free energy of binding between the ligand and the rhenium complex. The free energy in solution for the same transformation but calculated in the reverse

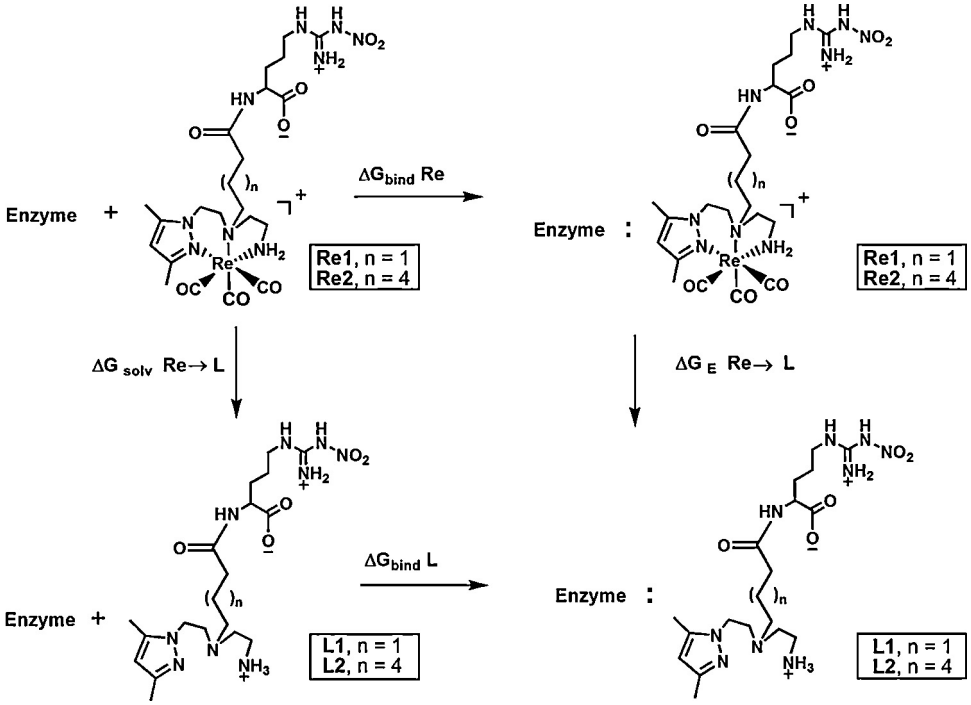

Fig. 11. Thermodynamic cycle for calculating the free binding energy difference between the rhenium complexes (**Re1**, $n = 1$; **Re2**, $n = 4$) and the respective ligands (**L1**, $n = 1$; **L2**, $n = 4$) bound to iNOS. Horizontal legs are determined experimentally and generally are not amenable to statistical simulations. Vertical transformations correspond to "alchemical transformations" of the Re complexes in the free state (left) and in the bound state (right). From the thermodynamic cycle it follows that the relative binding affinity $\Delta\Delta G_{bind}$ Re → L can be calculated using: $\Delta\Delta G_{bind}$ Re → L = ΔG_{bind} L − ΔG_{bind} Re = ΔG_E Re → L − ΔG_{solv} Re → L.

direction (ΔG_{solv} Re → L) was 31.29 kcal/mol, while bound to the protein (ΔG_E Re → L) was 29.69 kcal/mol, giving a $\Delta\Delta G_{bind}$ Re → L of −1.60 kcal/mol (Fig. 12). Overall the forward and backward FEP calculations show an average decrease of 1.825 ± 0.318 kcal/mol in the binding affinity upon the transformation of **Re2** into **L2**.

Despite the difference between the calculated $\Delta\Delta G_{bind}$ **Re → L** ($\Delta\Delta G_{bind}$ **Re1 → L1** = 0.690 ± 0.028 kcal/mol; $\Delta\Delta G_{bind}$ **Re2 → L2** = 1.825 ± 0.318 kcal/mol) and the experimental data ($\Delta\Delta G^{exp}_{bind}$ **Re1 → L1** = 0.461 ± 0.009 kcal/mol; ($\Delta\Delta G^{exp}_{bind}$ **Re2 → L2** = 1.129 ± 0.210 kcal/mol), the calculated values are

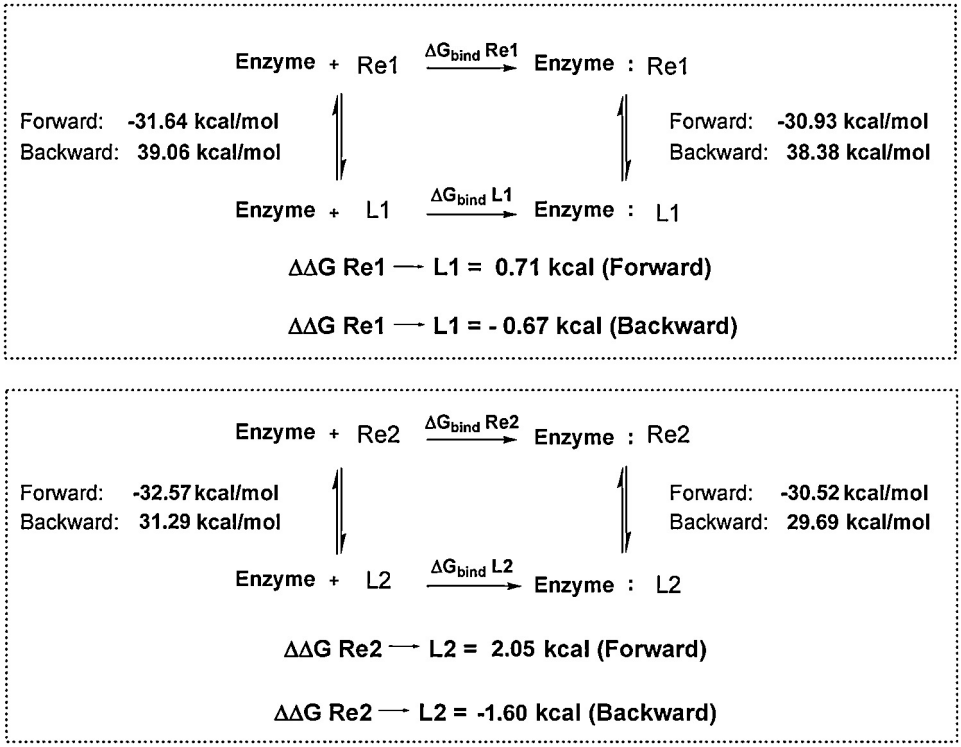

Fig. 12. Thermodynamic cycle representing the transformation of **Re1** into **L1** and **Re2** into **L2** in solution and bound to the protein.

Table 1
Calculated $\Delta\Delta G$ values for the transformation of **Re1** into **L1** and **Re2** into **L2**. Experimental $\Delta\Delta G$ values are also reported for comparison. Errors are estimated from forward and backward calculations. Experimental binding free energies (K_i values) were converted into ΔG (kcal/mol) as follows: $\Delta G_{bind} = k_B T \ln K_i$.

Transformation	$(\Delta\Delta G^{calc}_{bind}$ (kcal/mol)	$(\Delta\Delta G^{exp}_{bind}$ (kcal/mol)
Re1 → **L1**	0.690 ± 0.028	0.461 ± 0.009
Re2 → **L2**	1.825 ± 0.318	1.129 ± 0.210

sufficient to confirm that there is an energetic penalty when the Re complexes are transformed into the ligands. This penalty is higher for the pair **Re2/L2** (1.825 ± 0.318 kcal/mol) than for **Re1/L1** (0.690 ± 0.028 kcal/mol), a tendency which is also found in the experimental results ($\Delta\Delta G^{exp}_{bind}$ **Re2** → **L2** = 1.129 ± 0.210 and ($\Delta\Delta G^{exp}_{bind}$ **Re1** → **L1** = 0.461 ± 0.009). Despite the slight overestimation of the absolute binding free energy, our FEP calculations showed a good performance and a correct ranking of the inhibitiors studied. This fact, validates our docking/MD methodology and demonstrates that our structural conclusions were well retrieved for these systems. The validation of our methodology (docking, MD and FEP calculations) against experimental data suggests that the same approach can be applied with confidence in the future for designing novel rhenium complexes with higher capabilities.

3. Conclusion

Aiming to elucidate the effect of the structural parameters of **L1**, **L2**, **Re1** and **Re2** in their inhibitory potency, we have docked the compounds into the enzyme using the AutoDock software, which was previously validated with a set of X-ray structures of ligand:iNOS complexes. The best conformations of **L1**, **L2**, **Re1** and **Re2** obtained by docking were refined based on MD simulations. The decreased affinity of N^{ω}-NO_2-L-Arg toward iNOS, after conjugation to the pyrazolyl-diamine-containing chelator to give **L1** and **L2**, can be explained by the lost of strong H-bonding between its α-NH_3^+ group and the CO_2^- group of the heme propionate A. Upon metallation, the increased potency of the **Re1** and **Re2** complexes, compared to **L1** and **L2**, can be explained by the additional contacts observed between iNOS and the rhenium complexes. The higher inhibitory effect of **Re2** arises from the stronger electrostatic interactions observed between the "$Re(CO)_3$" core and the residues Arg260 and Arg382. This interaction, which is absent in the **Re1**:iNOS complex, is only possible due to the higher flexibility associated to the C6-carbon linker when compared to the C3 linker present in **Re1**. For **Re1**, the hydrophobic interactions between the pyrazolyl-diamine chelator and the hydrophobic pocket defined by Met114, Asn115, Pro116, Thr120 and Tyr485, combined with the interactions between the protein and the N^{ω}-NO_2-L-Arg moiety may account for its reasonable affinity. We have studied also the effect of the transformation of **Re1** into **L1** and **Re2** into **L2** on the binding affinity to iNOS using the FEP methodology. We have observed that the free energy differences match the trend observed in the experimental data: (1) there is an energetic penalty for the transformation of the Re complexes into the ligands; (2) the higher energetic penalty found experimentally for the pair **Re2**/**L2** was confirmed by FEP. These results suggest that the type of interactions observed between the inhibitors and iNOS are correct. These findings highlight the power of molecular modeling for structure and binding affinity predictions and its potential for structure-based drug design.

Brought together, our results demonstrated that molecular docking combined with MD simulations and FEP calculations showed a good performance and can be applied to predict the affinity of novel rhenium complexes prior to synthesizing them.

4. Methods

4.1. Molecular docking calculations

AutoDock4.2 was employed to perform protein-ligand docking calculations. The protein structure used in the docking studies were taken from the Research Collaboratory for Structural Bioinformatics (RCSB) protein database (pdb id code 1QW4; monomer A) [10]. A property of the AutoDock software is its ability to take into account the flexibility of the enzyme during the docking process. According to the literature, the most important residues of the iNOS enzyme for catalytic activity were considered fully flexible during the docking process (Gln257, Tyr341, Trp366, Tyr367, Glu371). To validate the accuracy of our docking conditions, we docked known inhibitors of iNOS (compounds **1**–**11**, Fig. S1) and compared the obtained conformation with the conformation found in the X-ray structure. The 3D structures of the inhibitors were extracted from the pdb structures (L-Arg, **1**, pdb id 1NOD [8]; N^{ω}-OH-L-Arg, **2**, pdb id 1DWV [9]; N^{ω}-propyl-L-Arg, **3**, pdb id 1QW4 [10]; L-thiocitrulline, **4**, pdb id 3NOD [9]; 4-fluoro-iminoethyl-L-lysine, **5**, pdb id 1R35 [11]; isothiourea, **6**, pdb id 1DF1 [18]; acetamidine, **7**, pdb id 1QW5 [10]; coumarin, **8**, pdb id 2BHJ [19]; nitroindazole, **9**, pdb id 1M8E [20]; quinazoline, **10**, pdb id 3E7T [12]; aminopyridine, **11**, pdb id 3EAI [12]). The rotatable bonds and the atomic partial charges (Gasteiger) were assigned by using AutoDock tools. All rotatable bonds in the ligands were kept free (except the ring systems) to allow for flexible docking. The protein-ligand complexes were prepared with AutoDockTools: For the protein hydrogen atoms were added and Kollman united atom charges were assigned. Hydrogens were also added to the ligands, heme and H_4B, and charges were calculated by the Gasteiger-Marsili method [33]. The Fe atom of heme was assigned a charge of +3. The ligands were docked inside a cubic grid box (48 Å × 32 Å × 58 Å) centered on the Fe atom of the heme group with a grid spacing of 0.375 Å. In each docking simulation 100 independent Lamarckian genetic algorithm (LGA) runs were performed, with the population size set to 200, the number of energy evaluations set to 10,000,000 and the maximum number of generations set to 27,000. All other parameters were maintained at their default settings [34,35]. The resulting docked conformations within a RMSD of 2 Å were clustered together. The lowest and more populated energy cluster returned by AutoDock that fulfilled some known structural criteria important for enzyme activity was used for conformational binding analysis. RMSD between the experimental and computational structures of the inhibitors were computed to evaluate the accuracy of the calculated poses.

In the case of the ligands (**L1** and **L2**) and the rhenium complexes (**Re1** and **Re2**), for which no X-ray structure is available, the validated method was used to predict their binding conformation inside the iNOS enzyme. The protonation state of the inhibitors at physiologic pH was determined with Epik 1.6 (Schrödinger) [36].

All rotatable bonds of the ligands **L1** and **L2** were kept free, with the exception of the rotatable bonds of the pyrazolyl ring and the N^{ω}-NO_2-L-Arg moiety, which was kept rigid in the same conformation found on the X-ray structure of this inhibitor complexed with nNOS (pdb id 1K2R) (Fig. S5). In the case of **Re1** and **Re2** the 3D-structure information of the pyrazolyl-diamine chelating unit, which stabilizes the *fac*-$[Re(CO)_3]^+$ core, was taken from the Cambridge Crystallographic Data Centre (CCDC reference number 789827) [37]. The docking experiments were carried out allowing **Re1** and **Re2** to rotate freely with the exception of the rotatable bonds of the pyrazolyl-diamine chelating unit and the N^{ω}-NO_2-L-Arg moiety (Fig. S5), which were kept in the conformation found in the X-ray structures. A charge of +1 was assigned for the Rhenium atom of **Re1** and **Re2**. The chosen complexes **L1**:iNOS, **L2**:iNOS, **Re1**:iNOS and **Re2**:iNOS were subjected to MD simulations.

4.2. MD simulations

DFT calculations have been shown to give very accurate results for systems involving transition metals [38]. Among the plethora of existing density functionals, we chose B3LYP that has been shown to be an appropriate choice for transition-metal complexes and rhenium specifically [39–43].

The geometries of the inhibitors **L1**, **L2**, **Re1** and **Re2** were optimized using the B3LYP/6-31G* level of theory with the Gaussian 09 program (version A.02), while charge fitting was performed using the RESP program [44,45]. The Molecular Electrostatic Potential (MEP) computations were carried out using the same level of theory and the Connolly surface algorithm [46]. In the case of the Re complexes it was used the B3LYP level of theory with the 6-31G* basis set for all atoms and the SDD basis set for Re. The SDD basis set uses the small core quasi-relativistic Stuttgart/Dresden electron core potentials for transition elements [47–49]. A spin multiplicity of 1, a charge of +1 and a radius of 1.47 Å for the Re(I) were considered in the DFT calculations. The charge derivation procedure was carried out using the R.E.D. (RESP ESP charge Derive) Server version 2.0 [50–52]. A detailed description of this procedure is reported in the Supporting Information (Figs. S9–S13). RESP atomic charges calculated for **L1**, **L2**, **Re1** and **Re2** are presented in Figs. S14–17.

To evaluate the ability of the chosen functional to reproduce the X-ray structures of the rhenium complexes, the bond lengths and angles of the optimized structures were compared with the corresponding values found in the experimental crystal structures (Table S2). The results have shown that both HF/6-31G*/SDD and B3LYP/6-31G*/SDD calculated values reproduce satisfactorily the X-ray crystal structures.

The topologies and parameters of the organic molecules (**L1** and **L2**) compatible with the CHARMM all atoms force field were derived from the ParamChem server (https://www.paramchem.org/) [42,53,54]. Parameters for the metal fragment were taken from previous parameterization studies of technetium and rhenium complexes [55–59]. All the dihedral parameters involving the Re–ligand interactions were set to zero. This procedure has been used with success in the treatment of several different systems that have a metal atom covalently bonded [60–62]. Lennard–Jones parameters are also not parameterized due to the fact that the Re metal is buried and that van der Waals interactions are not as important as the electrostatics [63]. Lennard–Jones parameters for the Re metal were taken from the literature [56].

Based on the docking results, MD simulations for compounds **L1**, **L2**, **Re1** and **Re2** were performed using NAMD [28] and CHARMM27 force fields [64]. The 3D-structure of iNOS was taken from pdb 1QW4 [10]. The MD simulations were set up as we described recently [13]. Briefly, the oxo-ferryl form (compound I) of heme, which has an oxygen atom at the sixth coordination position of iron, was used in the simulations. The force field parameters of the H_4B cofactor and compound I were kindly provided by Cho et al. [65]. The propKa module of the PDB2PQR server (http://kryptonite.nbcr.net/pdb2pqr/) was used to adjust the protonation states of ionizable residues at physiological pH [66–68]. Water molecules observed in the crystals structures were kept and additional TIP3P water molecules (box of dimension 10 Å × 10 Å × 10 Å) were modeled using the solvate package in VMD. Next, the systems were neutralized by adding counter ions with the autoionize package in VMD. The whole systems contained: **L1**:iNOS – 418 residues, 17102 water molecules and 1 Na^+ (58217 atoms total); **L2**:iNOS – 418 residues, 17072 water molecules and 5 Na^+ (58135 atoms total); **Re1**:NOS – 418 residues, 17070 water molecules and 3 Cl^- (58129 atoms total); **Re2**:NOS – 418 residues, 17064water molecules and 3 Cl^- (58120 atoms total).

All models were subjected to 3000 energy minimization steps and then simulations continued for another 8 ns. Rigid bonds were used for all hydrogen atoms, thus allowing a time step of 2 fs to be used. The force field parameters were kept standard as specified by the CHARMM force field. Short range nonbonded van der Waals interactions were computed every 2 fs, and the long-range electrostatic ones were computed every 4 fs. Starting from a switching distance of 10 Å, the Lennard–Jones potential was smoothly reduced to zero at a cut-off distance of 12 Å. The particle mesh Ewald (PME) method was employed for full electrostatics, with a grid point density of at least 1/Å^3 in all cases [69]. The simulations were performed in the NPT ensemble, using the Nosé–Hoover Langevin piston method for pressure control (1 atm), with an oscillation period of 200 fs and a damping time of 50 fs; constant temperature (T = 310 K) was enforced using Langevin dynamics with a damping coefficient of 5/ps on all nonhydrogen atoms [70–73].

Several detailed analyses were carried out for the trajectories obtained from the last 3 ns of the equilibrated simulations. The NAMD energy plugin of VMD was used to calculate the electrostatic interaction energies between protein and inhibitors for each snapshot of the MD trajectory. The water molecules, which were within 3 Å from the inhibitors in each snapshot were identified by using appropriate Tcl script executed within VMD, and the percentage of residence time calculated. The averaged-structures of the last 3 ns of the simulations were also calculated using appropriate Tcl script. All the pictures were made with the Pymol software [74].

4.3. Computational details for VolArea

The volumes of the active site cavities for **L1**:iNOS, **L2**:iNOS, **Re1**:iNOS and **Re2**:NOS, as well as the volume of the inhibitors **L1**, **L2**, **Re1** and **Re2** were calculated using the VolArea software with a box volume of 20.9, 18.7 and 25.5 Å^3 centered in a point between the heme propionates. The volumes were calculated using a probe radius of 1.0 Å [21].

4.4. Free energy calculations

The alchemical FEP transformations were performed using the dual-topology paradigm, in which the initial and the final states are defined in terms of distinct, non-interacting topologies, and the interactions of the transformed atoms with their environment are scaled in terms of a linear parameter, λ, often called coupling parameter [28,75]. In general, the atoms in the molecular topology are separated into three groups: (i) atoms which do not change during the simulation, (ii) the atoms describing the reference state, A, of the system, and (iii) the atoms that correspond to the target state, B, at the end of the alchemical transformation. The initial state was chosen to be the equilibrium state of the Re complexes **Re1** and **Re2**. The final state was set up such that the "$Re(CO)_3$" core in the complexes was vanished to give the ligands **L1** and **L2**. The energy and forces in the FEP simulations were defined such that the interaction of the "$Re(CO)_3$" core in the initial state with the rest of the system is effective at the beginning of the simulation (λ = 0), and nonexistent at the end of the simulation (λ = 1). In a typical FEP calculation for a transformation from state A to state B, many λ are needed in order to obtain a smooth transition from the initial state A to the final state B. A source of error in a FEP calculation involves the end points of the transformation. Due to the appearing and disappearing atoms, van der Waals' clashes occur and result in "end point catastrophes", which prevent correct convergence of the calculation [76]. A number of schemes have been devised to circumvent this problem, among which the increasing of the number of intermediate λ states in the calculation to decrease the conformational difference between consecutive λ states [77,78]. To obtain an

accurate estimate of the free energy, we increased the number of windows at the beginning and end of the FEP simulations, collecting data at several points with λ values close to zero or one. The bound (soft-core) vdW potential was also used to repel all overlapping particles when λ tends toward either 0 or 1 [78–80].

The averaged structures of the complexes **Re1**:iNOS and **Re2**:iNOS calculated for the last 3 ns of simulation were used as starting points for FEP calculations. Several different simulation schemes were tried in order to find conditions that produced converging energy results with minimal dispersion. It was observed that the use of 24 intermediate states (0.0000001, 0.000001, 0.00001, 0.0001, 0.001, 0.01, 0.05, 0.1; between 0.1 and 0.9 the change in λ was linear with a Δλ of 0.1; at the final segments the progression of λ was 0.9, 0.95, 0.99, 0.999, 0.9999, 0.99999, 0.999999, 0.9999999) and simulations times of 0.28 ns were not enough to obtain convergence. In order to achieve convergence each FEP calculation was split into more intermediate λ states (0.0000001, 0.000001, 0.00001, 0.0001, 0.001, 0.01, 0.05, 0.1; between 0.1 and 0.9 the change in λ was linear with a Δλ of 0.05; at the final segments the progression of λ was 0.9, 0.95, 0.99, 0.999, 0.9999, 0.99999, 0.999999, 0.9999999) and the simulation time was increased. At each intermediate λ state, equilibration was run for 24 ps, followed by 240 ps of FEP data collection. The extra intermediate states and the use of more steps for equilibration and acquisition at each λ increased the total length of the FEP simulation to 8.45 ns. To check the dependency of the results on the direction of the transformation, the free energy profiles of the backward transformation were also calculated. Considering the simulations in both free and bound states, as well as in the forward and backward directions, the total time of simulation was ~33 ns.

Acknowledgements

This work was funded by the Fundação para a Ciência e Tecnologia (FCT), Portugal (PTDC/QUI-QUI/121752/2010). We would like to thank F.-Y. Dupradeau for advice on using the R.E.D. server and for helpful discussions.

Appendix A. Supplementary data

Supplementary data associated with this article can be found, in the online version, at http://dx.doi.org/10.1016/j.jmgm.2013.07.007.

References

[1] W.K. Alderton, R.G. Knowles, Nitric oxide synthases: structure, function and inhibition, Biochemistry Journal 357 (2001) 593–615.
[2] U. Grädler, T. Fuchß, W.-R. Ulrich, R. Boer, A. Strub, C. Hesslinger, et al., Novel nanomolar imidazo[4,5-b]pyridines as selective nitric oxide synthase (iNOS) inhibitors: SAR and structural insights, Bioorganic & Medicinal Chemistry Letters 21 (2011) 4228–4232.
[3] P. Vallance, J. Leiper, Blocking NO synthesis: how, where and why, Nature Reviews Drug Discovery 1 (2002) 939–950.
[4] B.L. Oliveira, P.D. Raposinho, F. Mendes, I.C. Santos, I. Santos, A. Ferreira, et al., Targeting nitric oxide synthase with 99mTc/Re-tricarbonyl complexes containing pendant guanidino or isothiourea moieties, Journal of Organometallic Chemistry 696 (2011) 1057–1065.
[5] B.L. Oliveira, P.D. Raposinho, F. Mendes, FigueiraS F.V., I. Santos, A.N. Ferreira, et al., Re and Tc tricarbonyl complexes: from the suppression of NO biosynthesis in macrophages to in vivo targeting of inducible nitric oxide synthase, Bioconjugate Chemistry 21 (2010) 2168–2172.
[6] B.L. Oliveira, J.D.G. Correia, P.D. Raposinho, I. Santos, A. Ferreira, C. Cordeiro, et al., Re and 99mTc organometallic complexes containing pendant L-arginine derivatives as potential probes of inducible nitric oxide synthase, Dalton Transactions 15 (2009) 2–62.
[7] A.C. Wallace, R.A. Laskowski, J.M. Thornton, LIGPLOT: a program to generate schematic diagrams of protein–ligand interactions, Protein Engineering 8 (1995) 127–134.
[8] B.R. Crane, A.S. Arvai, S. Ghosh, E.D. Getzoff, D.J. Stuehr, J.A. Tainer, Structures of the Nω-hydroxy-L-arginine complex of inducible nitric oxide synthase oxygenase dimer with active and inactive pterins, Biochemistry 39 (2000) 4608–4621.
[9] B.R. Crane, A.S. Arvai, D.K. Ghosh, C. Wu, E.D. Getzoff, D.J. Stuehr, et al., Structure of nitric oxide synthase oxygenase dimer with pterin and substrate, Science 279 (1998) 2121–2126.
[10] R. Fedorov, E. Hartmann, D.K. Ghosh, I. Schlichting, Structural basis for the specificity of the nitric-oxide synthase inhibitors W1400 and Nω-propyl-L-Arg for the inducible and neuronal isoforms, Journal of Biological Chemistry 278 (2003) 45818–45825.
[11] E. Ann Hallinan, S.W. Kramer, S.C. Houdek, W.M. Moore, G.M. Jerome, D.P. Spangler, et al., 4-Fluorinated L-lysine analogs as selective i-NOS inhibitors: methodology for introducing fluorine into the lysine side chain, Organic and Biomolecular Chemistry 1 (2003) 3527–3534.
[12] E.D. Garcin, A.S. Arvai, R.J. Rosenfeld, M.D. Kroeger, B.R. Crane, G. Andersson, et al., Anchored plasticity opens doors for selective inhibitor design in nitric oxide synthase, Nature Chemical Biology 4 (2008) 700–707.
[13] B. Oliveira, I. Moreira, P. Fernandes, M. Ramos, I. Santos, J.G. Correia, Insights into the structural determinants for selective inhibition of nitric oxide synthase isoforms, Journal of Molecular Modeling 19 (2012) 1537–1551.
[14] F. Xue, J. Huang, H. Ji, J. Fang, H. Li, P. Martasek, et al., Structure-based design, synthesis, and biological evaluation of lipophilic-tailed monocationic inhibitors of neuronal nitric oxide synthase, Bioorganic & Medicinal Chemistry 18 (2010) 6526–6537.
[15] C. Maccallini, A. Patruno, N. Besker, J. Isabella, A. Ammazzalorso, B. de Filippis, et al., Synthesis, biological evaluation, and docking studies of N-substituted acetamidines as selective inhibitors of inducible nitric oxide synthase, Journal of Medicinal Chemistry 52 (2009) 1481–1485.
[16] S.M. Francis, A. Mittal, M. Sharma, P. Bharatam, Design of benzene-1,2-diamines as selective inducible nitric oxide synthase inhibitors: a combined de novo design and docking analysis, Journal of Molecular Modeling 14 (2008) 215–224.
[17] V. Aparna, G. Desiraju, B. Gopalakrishnan, Insights into ligand selectivity in nitric oxide synthase isoforms: a molecular dynamics study, Journal of Molecular Graphics and Modelling 26 (2007) 457–470.
[18] B.R. Crane, R.J. Rosenfeld, A.S. Arvai, D.K. Ghosh, S. Ghosh, J.A. Tainer, et al., N-terminal domain swapping and metal ion binding in nitric oxide synthase dimerization, EMBO Journal 18 (1999) 6271–6281.
[19] S.A. Jackson, S. Sahni, L. Lee, Y. Luo, T.R. Nieduzak, G. Liang, et al., Design, synthesis and characterization of a novel class of coumarin-based inhibitors of inducible nitric oxide synthase, Bioorganic and Medicinal Chemistry 13 (2005) 2723–2739.
[20] R.J. Rosenfeld, E.D. Garcin, K. Panda, G. Andersson, A. Åberg, A.V. Wallace, et al., Conformational changes in nitric oxide synthases induced by chlorzoxazone and nitroindazoles: crystallographic and computational analyses of inhibitor potency, Biochemistry 41 (2002) 13915–13925.
[21] VolArea, João Ribeiro, Group of Computational BioChemistry, Faculty of Sciences of the University of Porto, Porto, Portugal, 2013, http://www.compbiochem.org/Software/Volarea/Home.html
[22] G. Steinkellner, R. Rader, G. Thallinger, C. Kratky, K. Gruber, VASCo: computation and visualization of annotated protein surface contacts, BMC Bioinformatics 10 (2009) 32.
[23] C.-E.A. Chang, W. Chen, M.K. Gilson, Ligand configurational entropy and protein binding, Proceedings of the National Academy of Sciences 104 (2007) 1534–1539.
[24] D.L. Mobley, K.A. Dill, Binding of small-molecule ligands to proteins: what you see is not always what you get, Structure 17 (2009) 489–498.
[25] C. Gao, M.-S. Park, H.A. Stern, Accounting for ligand conformational restriction in calculations of protein–ligand binding affinities, Biophysical Journal 98 (2010) 901–910.
[26] E. Perola, P.S. Charifson, Conformational analysis of drug-like molecules bound to proteins: an extensive study of ligand reorganization upon binding, Journal of Medicinal Chemistry 47 (2004) 2499–2510.
[27] C. Diehl, O. Engström, T. Delaine, M. Håkansson, S. Genheden, K. Modig, et al., Protein flexibility and conformational entropy in ligand design targeting the carbohydrate recognition domain of galectin-3, Journal of the American Chemical Society 132 (2010) 14577–14589.
[28] J.C. Phillips, R. Braun, W. Wang, J. Gumbart, E. Tajkhorshid, E. Villa, et al., Scalable molecular dynamics with NAMD, Journal of Computational Chemistry 26 (2005) 1781–1802.
[29] W. Humphrey, A. Dalke, K.V.M.D. Schulten, Visual molecular dynamics, Journal of Molecular Graphics 14 (1996) 33–38.
[30] M.A.S. Perez, P.A. Fernandes, M.J. Ramos, Substrate recognition in HIV-1 protease: a computational study, Journal of Physical Chemistry B 114 (2010) 2525–2532.
[31] D.A. Pearlman, A comparison of alternative approaches to free energy calculations, Journal of Physical Chemistry 98 (1994) 1487–1493.
[32] J. Hénin, C. Harrison, C. Chipot, A Tutorial for Alchemical FEP in NAMD, vol. 2011, 2010.
[33] J. Gasteiger, M. Marsili, Iterative partial equalization of orbital electronegativity—a rapid access to atomic charges, Tetrahedron 36 (1980) 3219–3228.
[34] G.M. Morris, D.S. Goodsell, R.S. Halliday, R. Huey, W.E. Hart, R.K. Belew, et al., Automated docking using a Lamarckian genetic algorithm and an empirical binding free energy function, Journal of Computational Chemistry 19 (1998) 1639–1662.

[35] G.M. Morris, R. Huey, W. Lindstrom, M.F. Sanner, R.K. Belew, D.S. Goodsell, et al., AutoDock4 and AutoDockTools4: automated docking with selective receptor flexibility, Journal of Computational Chemistry 30 (2009) 2785–2791.
[36] J. Shelley, A. Cholleti, L. Frye, J. Greenwood, M. Timlin, M. Uchimaya, Epik: a software program for pKa prediction and protonation state generation for drug-like molecules, Journal of Computer-Aided Molecular Design 21 (2007) 681–691.
[37] E. Palma, J.D.G. Correia, B.L. Oliveira, L. Gano, I.C. Santos, I. Santos, 99mTc(CO)3-labeled pamidronate and alendronate for bone imaging, Dalton Transactions 40 (2011) 2787–2796.
[38] T. Ziegler, Approximate density functional theory as a practical tool in molecular energetics and dynamics, Chemical Reviews 91 (1991) 651–667.
[39] A.D. Becke, Density-functional thermochemistry. III. The role of exact exchange, Journal of Chemical Physics 98 (1993) 5648–5652.
[40] S.F. Sousa, P.A. Fernandes, M.J. Ramos, General performance of density functionals, Journal of Physical Chemistry A 111 (2007) 10439–10452.
[41] C. Lee, W. Yang, R.G. Parr, Development of the Colle-Salvetti correlation-energy formula into a functional of the electron density, Physical Review B 37 (1988) 785.
[42] K. Vanommeslaeghe, E. Hatcher, C. Acharya, S. Kundu, S. Zhong, J. Shim, et al., CHARMM general force field: a force field for drug-like molecules compatible with the CHARMM all-atom additive biological force fields, Journal of Computational Chemistry 31 (2010) 671–690.
[43] X. Li, X. Liu, Z. Wu, H. Zhang, DFT/TDDFT studies on the electronic structures and spectral properties of rhenium(I) pyridinybenzoimidazole complexes, Journal of Physical Chemistry A 112 (2008) 11190–11197.
[44] C.I. Bayly, P. Cieplak, W. Cornell, P.A. Kollman, A well-behaved electrostatic potential based method using charge restraints for deriving atomic charges: the RESP model, Journal of Physical Chemistry 97 (1993) 10269–10280.
[45] W.D. Cornell, P. Cieplak, C.I. Bayly, P.A. Kollmann, Application of RESP charges to calculate conformational energies, hydrogen bond energies, and free energies of solvation, Journal of the American Chemical Society 115 (1993) 9620–9631.
[46] M. Connolly, Analytical molecular surface calculation, Journal of Applied Crystallography 16 (1983) 548–558.
[47] D. Andrae, U. Häußermann, M. Dolg, H. Stoll, H. Preuß, Energy-adjusted ab initio pseudopotentials for the second and third row transition elements, Theoretical Chemistry Accounts: Theory, Computation, and Modeling (Theoretica Chimica Acta) 77 (1990) 123–141.
[48] T.H. Dunning Jr., P.J. Hay, Modern Theoretical Chemistry, vol. 3, Plenum, New York, 1976, pp. 1–28.
[49] M. Dolg, H. Stoll, H. Preuss, Energy-adjusted ab initio pseudopotentials for the first row transition elements, Journal of Chemical Physics 86 (1987) 866–873.
[50] F.-Y. Dupradeau, A. Pigache, T. Zaffran, C. Savineau, R. Lelong, N. Grivel, et al., The R.E.D. tools: advances in RESP and ESP charge derivation and force field library building, Physical Chemistry Chemical Physics 12 (2010) 7821–7839.
[51] F.-Y. Dupradeau, C. Cézard, R. Lelong, É. Stanislawiak, J. Pêcher, J.C. Delepine, et al., R.E.DD.B.: a database for RESP and ESP atomic charges, and force field libraries, Nucleic Acids Research 36 (2008) D360–D367.
[52] E. Vanquelef, S. Simon, G. Marquant, E. Garcia, G. Klimerak, J.C. Delepine, et al., R.E.D. Server: a web service for deriving RESP and ESP charges and building force field libraries for new molecules and molecular fragments, Nucleic Acids Research 39 (2011) W511–W517.
[53] K. Vanommeslaeghe, A.D. MacKerell, Automation of the CHARMM General Force Field (CGenFF) I: bond perception and atom typing, Journal of Chemical Information and Modeling 52 (2012) 3144–3154.
[54] K. Vanommeslaeghe, E.P. Raman, A.D. MacKerell, Automation of the CHARMM General Force Field (CGenFF) II: assignment of bonded parameters and partial atomic charges, Journal of Chemical Information and Modeling 52 (2012) 3155–3168.
[55] D.E. Reichert, M.J. Welch, Applications of molecular mechanics to metal-based imaging agents, Coordination Chemistry Reviews 212 (2001) 111–131.
[56] P. Wolohan, D.E. Reichert, CoMSIA and docking study of rhenium based estrogen receptor ligand analogs, Steroids 72 (2007) 247–260.
[57] M. Stichelberger, D. Desbouis, V. Spiwok, L. Scapozza, P.A. Schubiger, R. Schibli, Synthesis, in vitro and in silico assessment of organometallic rhenium(I) and technetium(I) thymidine complexes, Journal of Organometallic Chemistry 692 (2007) 1255–1264.
[58] Desbouis, D. Struthers, H. Spiwok, V. Küster, T. Schibli, R. Synthesis, In vitro, and in silico evaluation of organometallic technetium and rhenium thymidine complexes with retained substrate activity toward human thymidine kinase type 1, Journal of Medicinal Chemistry 51 (2008) 6689–6698.
[59] S. James, K.P. Maresca, D.G. Allis, J.F. Valliant, W. Eckelman, J.W. Babich, et al., Extension of the single amino acid chelate concept (SAAC) to bifunctional biotin analogues for complexation of the M(CO)3 + 1 core (M = Tc and Re): syntheses, characterization, biotinidase stability, and avidin binding, Bioconjugate Chemistry 17 (2006) 579–589.
[60] S.C. Hoops, K.W. Anderson, K.M. Merz, Force field design for metalloproteins, Journal of the American Chemical Society 113 (1991) 8262–8270.
[61] M.B. Peters, Y. Yang, B. Wang, L.S. Füsti-Molnár, M.N. Weaver, K.M. Merz, Structural survey of zinc-containing proteins and development of the zinc AMBER force field (ZAFF), Journal of Chemical Theory and Computation 6 (2010) 2935–2947.
[62] S. Sousa, P. Fernandes, M. Ramos, Effective tailor-made force field parameterization of the several Zn coordination environments in the puzzling FTase enzyme: opening the door to the full understanding of its elusive catalytic mechanism, Theoretical Chemistry Accounts: Theory, Computation, and Modeling (Theoretica Chimica Acta) 117 (2007) 171–181.
[63] P.-O. Norrby, P. Brandt, Deriving force field parameters for coordination complexes, Coordination Chemistry Reviews 212 (2001) 79–109.
[64] A.D. MacKerell, D. Bashford, R.L. Bellott Dunbrack, J.D. Evanseck, M.J. Field, et al., All-atom empirical potential for molecular modeling and dynamics studies of proteins, Journal of Physical Chemistry B 102 (1998) 3586–3616.
[65] K.-B. Cho, E. Derat, S. Shaik, Compound I of nitric oxide synthase: the active site protonation state, Journal of the American Chemical Society 129 (2007) 3182–3188.
[66] T.J. Dolinsky, J.E. Nielsen, J.A. McCammon, N.A. Baker, PDB2PQR: an automated pipeline for the setup of Poisson–Boltzmann electrostatics calculations, Nucleic Acids Research 32 (2004) W665–W667.
[67] T.J. Dolinsky, P. Czodrowski, H. Li, J.E. Nielsen, J.H. Jensen, G. Klebe, et al., PDB2PQR: expanding and upgrading automated preparation of biomolecular structures for molecular simulations, Nucleic Acids Research 35 (2007) W522–W525.
[68] H. Li, A.D. Robertson, J.H. Jensen, Very fast empirical prediction and rationalization of protein pKa values, Proteins: structure, function, and bioinformatics 61 (2005) 704–721.
[69] U. Essmann, L. Perera, M.L. Berkowitz, T. Darden, H. Lee, L.G. Pedersen, A smooth particle mesh Ewald method, Journal of chemical physics 103 (1995) 8577–8593.
[70] W.G. Hoover, Canonical dynamics: equilibrium phase-space distributions, Physical Review A 31 (1985) 1695.
[71] S.E. Feller, Y. Zhang, R.W. Pastor, B.R. Brooks, Constant pressure molecular dynamics simulation: the Langevin piston method, Journal of Chemical Physics 103 (1995) 4613–4621.
[72] S. Nosé, A molecular dynamics method for simulations in the canonical ensemble, Molecular Physics: An International Journal at the Interface Between Chemistry and Physics 100 (2002) 191–198.
[73] G.S. Grest, K. Kremer, Molecular dynamics simulation for polymers in the presence of a heat bath, Physical Review A 33 (1986) 3628.
[74] W.L. DeLano, The PyMOL Molecular Graphics System, DeLano Scientific, San Carlos, CA, USA, 2002.
[75] M. Bhandarkar, R. Brunner, C. Chipot, A. Dalke, S. Dixit, NAMD User's Guide, Version 2.6b1., Theoretical Biophysics Group, University of Illinois and Beckman Institute, Urbana, IL, 2005.
[76] J.W. Pitera, W.F. van Gunsteren, A comparison of non-bonded scaling approaches for free energy calculations, Molecular Simulation 28 (2002) 45–65.
[77] C. Chipot, D.A. Pearlman, Free energy calculations. The long and winding gilded road, Molecular Simulation 28 (2002) 1–12.
[78] A. Pohorille, C. Jarzynski, C. Chipot, Good practices in free-energy calculations, Journal of Physical Chemistry B 114 (2010) 10235–10253.
[79] M. Zacharias, T.P. Straatsma, J.A. McCammon, Separation shifted scaling, a new scaling method for Lennard-Jones interactions in thermodynamic integration, The Journal of Chemical Physics 100 (1994) 9025–9031.
[80] T.C. Beutler, A.E. Mark, R.C. van Schaik, P.R. Gerber, W.F. van Gunsteren, Avoiding singularities and numerical instabilities in free energy calculations based on molecular simulations, Chemical Physics Letters 222 (1994) 529–539.